



# Demography of Stellar Radio Population within 500 pc: A VLASS-Gaia DR3 Study

D. Ayanabha<sup>1</sup>, Mayank Narang<sup>2</sup>, Manoj Puravankara<sup>1</sup>, B. Shridharan<sup>1</sup>, H. Tyagi<sup>1</sup>, Bihan Banerjee<sup>1</sup>,  
Prasanta K. Nayak<sup>3</sup>, and Arun Surya<sup>4</sup>

<sup>1</sup> Department of Astronomy & Astrophysics, Tata Institute of Fundamental Research, Homi Bhabha Road, Colaba, Mumbai, 400005, India; [astronomerrik@gmail.com](mailto:astronomerrik@gmail.com)

<sup>2</sup> Academia Sinica Institute of Astronomy & Astrophysics, 11F of Astro-Math Bldg., No. 1, Sec. 4, Roosevelt Rd., Taipei 10617, Taiwan, R.O.C.; [mayankn1154@gmail.com](mailto:mayankn1154@gmail.com)

<sup>3</sup> Instituto de Astrofísica, Pontificia Universidad Católica de Chile, Av. Vicuña MacKenna 4860, 7820436, Santiago, Chile

<sup>4</sup> Indian Institute of Astrophysics, 2nd block Koramangala, Bangalore, 560034, India

Received 2024 August 5; revised 2024 September 26; accepted 2024 September 26; published 2024 November 28

## Abstract

In this work, we have carried out a systematic analysis of the Very Large Array Sky Survey (VLASS) quick look catalogs together with Gaia DR3 to identify the optical counterparts of 3 GHz radio emitters within 500 pc to obtain a homogeneous statistical sample of stellar radio sources. We have identified distinct populations of 3 GHz emitters across the Gaia DR3 color–magnitude diagram. We also present candidate sources (transient, highly variable, or background artifacts) that can be confirmed by follow-up observations. A majority of the detected sources constitute main-sequence G-, K-, and M-type stars, including ultracool dwarfs. Pinning down the origin of radio emission from these populations can help us gain further insights into the origin of stellar and planetary magnetic fields. By analyzing the variation of brightness temperature of the sources with their spectral type, we have tentatively associated possible emission mechanisms with different object types. We inspected the correlation between quiescent radio and X-ray emission for our sample, which can provide crucial insights into the current understanding of the Gudel–Benz relationship, which is essential for modeling steady radio emission and coronal heating. This VLASS-Gaia DR3 analysis acts as a pilot study for follow-up observations at multiple wavelengths to better understand stellar structure, model flaring activities, and detect radio emission caused by star–planet interactions.

*Unified Astronomy Thesaurus concepts:* [Radio continuum emission \(1340\)](#); [Stellar magnetic fields \(1610\)](#); [Radio source catalogs \(1356\)](#); [Stellar properties \(1624\)](#); [Gaia \(2360\)](#); [Radio astronomy \(1338\)](#)

*Materials only available in the [online version of record](#): machine-readable table*

## 1. Introduction

Radio emission from stars and substellar objects offers a unique window into their physical characteristics, magnetic fields, and interaction with their surroundings. Observations across different wavelengths, along with modeling the emission, can contribute significantly to our understanding of these objects. By analyzing near-simultaneous observations at multiple frequencies across several epochs at radio wavelengths, plasma and magnetic field properties in the stellar surroundings and emission mechanisms can be studied (G. A. Dulk 1985; M. Gudel 2002). Radio observations can probe the stellar chromospheres, coronae, winds, and accretion around stars and young stellar objects (YSOs; A. J. Bookbinder 1988; H. K. Vedantham 2020; B. Das et al. 2022). Radio observation is also the only unambiguous method for detecting exoplanet magnetic fields (E. Shkolnik et al. 2008; P. W. Cauley et al. 2019; M. Narang et al. 2020).

The radio brightness temperature (defined in Section 4.1), along with effective temperature measurements of the source and spectral index estimates, can help us derive the nature of emission and source optical depth (M. Gudel 2002). A study of how the emission properties vary across different spectral and

object types can shed light on the physics of stellar structure and evolution.

Stellar radio emission results from various physical processes associated with different objects and spectral types. Nonthermal radio emission in main-sequence (MS) low-mass ( $0.5M_{\odot} \leq M_* \leq 1.5M_{\odot}$ , i.e., late-F-to-early-M-type) stars is mostly driven by persistent magnetic activity generated as a result of the presence of a tachocline (boundary between radiative and convective layers) and differential rotation in the outer convective layer (B. Dorman et al. 1989). The presence of a magnetic field in late M dwarfs and brown dwarfs is not well understood since they lack a tachocline (G. Chabrier & I. Baraffe 2000). Large-scale magnetospheric dynamics are likely the origin of radio emission from M dwarfs and brown dwarfs (T. W. H. Yiu et al. 2024). Hot B-, A-, and early F-type stars ( $M_* \geq 1.5M_{\odot}$ ) with almost entirely radiative interiors have no intrinsic magnetic fields (J. F. Donati & J. D. Landstreet 2009). However, there are magnetic chemically peculiar (MCP) stars that might have retained their fossil magnetic fields. Radio emission from such stars is possibly wind driven (A. E. Wright & M. J. Barlow 1975).

Close-in exoplanets can form Jupiter-Io like systems with their host stars (R. D. Kavanagh et al. 2021), thus providing a method to measure exoplanetary magnetic fields (J.-M. Grießmeier 2015). Search for such emissions is an active field in radio astronomy (e.g., A. Lecavelier Des Etangs & S. K. Sirothia 2011; H. K. Vedantham et al. 2020; M. Narang et al. 2020, 2021; C. Trigilio et al. 2023; K. N. O. Ceballos et al. 2024;

M. Narang et al. 2024). Similar to Jupiter–Io coupling (P. Goldreich & D. Lynden-Bell 1969), an exomoon can trigger activity in the magnetosphere of its host exoplanet, generating low-frequency radio emission (J. P. Noyola et al. 2014; M. Narang et al. 2023a, 2023b).

To study the origin and properties of stellar radio emission from various object types, several targeted observations and surveys have been carried out. For example, R. L. Mutel et al. (1985) carried out a survey to observe radio bursts from RS Canum Venaticorum (RS CVn) and Algol binaries. Similarly, F. Leone et al. (1996) and B. Das et al. (2022) carried out extensive observations of MCP stars to detect radio emissions from them. A. Feeney-Johansson et al. (2021) detected coherent bursts from weak-line T Tauri stars. Emission from the corona of the M dwarf WX Uma was studied in a target-specific observation by I. Davis et al. (2021). Volume-limited radio surveys have been carried out for OB-type radio stars (e.g., J. H. Bieging et al. 1989) and for ultracool dwarfs (e.g., E. Berger 2002; A. Antonova et al. 2013).

Targeted radio observations can be biased toward known radio-bright sources. To study the statistical properties of different radio populations, volume-limited unbiased wide-field sky surveys are necessary. Wide-field surveys like the Faint Images of the Radio Sky at Twenty-one centimeters (FIRST; R. H. Becker et al. 1995), the NRAO VLA Sky Survey (NVSS; J. J. Condon et al. 1998), the TIFR GMRT Sky Survey (TGSS; H. T. Intema et al. 2017), and the Westerbork Northern Sky Survey (WENSS; R. B. Rengelink et al. 1997) have detected and characterized many new radio objects (A. E. Kimball & U. Ivezić 2008; A. E. Kimball et al. 2009). However, the low angular resolution and sensitivity and large astrometric uncertainties of these sky surveys increase the probability of chance alignment with background galaxies and false detection of artifacts (e.g., A. E. Kimball et al. 2009) and require extensive follow-up (e.g., M. Narang 2022). The Very Large Array Sky Survey (VLASS; M. Lacy et al. 2020), the Rapid ASKAP Continuum Survey (RACS; D. McConnell et al. 2020), the LoFAR Two Meter Sky Survey (LoTSS; T. W. Shimwell et al. 2017), and the Galactic and Extra-galactic all-sky MWA survey (GLEAM; R. B. Wayth et al. 2015) are some of the recent radio surveys with higher sensitivity, astrometric accuracy, and increased resolution, which should reduce chance alignment probabilities and false detections.

Using the catalogs published from the aforementioned surveys, recent works have identified new radio stars (L. N. Driessen et al. 2023) and compiled new catalogs for megahertz to gigahertz stellar radio sources (T. W. H. Yiu et al. 2024; L. N. Driessen et al. 2024). Most of the sources identified through their analysis are low-frequency emitters. VLASS provides a window into the decimetric radio sky, where we expect many magnetic stars to emit gyrosynchrotron radio waves and YSOs to be present (M. Güdel 2002). T. W. H. Yiu et al. (2024) conducted a statistical analysis of certain stellar populations and their properties using VLASS, LoTSS, and the Gaia Catalog of Nearby Stars (GCNS; Gaia Collaboration et al. 2021). However, their analysis focused on studying the variation of detection rates with spectral types, so they limited their sample to a 50 pc volume in which GCNS is complete for all objects earlier than M8. This sample primarily consists of M dwarfs, for which they derived flare statistics.

In this work, we aim to study the general properties of a broad range of radio emitters—ranging from ultracool dwarfs

to hot B types, from binary systems to YSOs. For this investigation we use the first two-epoch data of VLASS along with Gaia DR3 to identify radio population within 500 pc. Such a large sample based on homogeneous selection criteria covering diverse spectral types allows us to study the nature of emission and their variation across different spectral and object types. Two epochs of observation separated by 32 months with the same sensitivity also allow variability studies. Our study focuses on identifying diverse populations of radio-emitting stellar systems in decimetric wavelength bands and characterizing the origin of their emission. We discuss stellar radio emission in the context of stellar structure and environment. In Section 2 we describe the data sets used in the paper and filtering methods. Our analysis and results are presented in Section 3, and we discuss our results in Section 4. Section 5 provides a summary of the paper.

## 2. Data and Sample Selection

VLASS is a National Radio Astronomy Observatory (NRAO) initiative to carry out a continuum survey of the entire sky above a decl. of  $-40^\circ$ , using the Karl G. Jansky Very Large Array in B and BnA configuration at S band (2–4 GHz; M. Lacy et al. 2020). The project, which was initiated in 2017 and is scheduled for completion by 2024, encompasses three distinct epochs of observation, each separated by an approximate interval of 32 months. The survey has rms noise of  $120 \mu\text{Jy}$  per epoch and an estimated  $60 \mu\text{Jy}$  rms noise for the three-epoch stacked images with an angular resolution of  $\sim 2''$ . Gaia is an ESA all-sky survey mission (Gaia Collaboration et al. 2023) that provides most precise astrometric and spectrophotometric measurements for  $\sim 1.7$  billion stars in the optical band.

In this work, we have crossmatched the Gaia Third Data Release (DR3) catalog (Gaia Collaboration et al. 2023) and VLASS Epoch 1 and 2 Quick Look (QL1 and QL2) catalogs (Y. A. Gordon et al. 2020) to identify the optical counterparts of the 3 GHz radio sources within 500 pc using precise parallax measurement from Gaia DR3. The QL catalogs, produced from minimally cleaned images, are well suited for demographic studies of radio stellar populations. More deeply cleaned and self-calibrated single-epoch (SE) images also provide in-band spectral index information, but due to their current incompleteness across the entire VLASS footprint, they are not used in this study. The combination of Gaia DR3 and VLASS QL catalogs provides us with a large-enough volume-limited homogeneous sample to study the demographics of emission properties of the stellar radio population across all spectral and object types. To reduce the possibilities of false associations of radio emitters with background galaxies detected by Gaia, we only consider sources with *parallax\_over\_error*  $> 10$ . This ensures that we have removed sources with bad parallax measurements.

The first epoch of VLASS observations was carried out from 2017 September to 2019 July, and the second epoch was carried out from 2020 April to 2022 April. Thus, the mean epoch for VLASS QL1 is 2018.7 and that for VLASS QL2 is 2021.33. The positions of Gaia DR3 sources, whose epoch is J2016, were proper motion corrected to J2018.7 and J2021.33. In the catalog user guide,<sup>5</sup> the positions of VLASS and Gaia DR2 (A. G. A. Brown et al. 2018) sources after epoch

<sup>5</sup> of the VLASS Quick Look and Single Epoch Catalogs web-page.

correction were compared to derive typical astrometric offsets in VLASS catalogs of  $\sim 0''.5$  above  $-20^\circ$  decl. and up to  $1''$  between  $-20^\circ$  and  $-40^\circ$  declination. Therefore, we consider a search radius of  $1''$  to account for the VLASS astrometric offset and epoch uncertainties due to proper motions up to  $0''.5 \text{ yr}^{-1}$ . Limiting ourselves to a  $1''$  search radius reduces the number of background radio components chance-aligning with a Gaia DR3 source. Using this strategy, however, we can miss sources with proper motion  $\gtrsim 0''.5 \text{ yr}^{-1}$  (see Section 2.1).

Radio galaxies and artifacts present in VLASS catalogs can align by chance with Gaia DR3 objects within the limited search radius. Artifacts can be filtered using data flags (explained in Section 2.2). To bypass chance alignments with uncatalogued galaxies, several methods can be employed. Identification by filtering polarized sources (J. Pritchard et al. 2021; J. R. Callingham et al. 2021) is biased to polarized radio sources. Serendipitous searches (L. N. Driessen et al. 2021; A. Andersson et al. 2022) are biased toward highly variable sources. Proper-motion searches have no bias toward properties of emission (L. N. Driessen et al. 2023). However, the volume limit of the proper-motion search relies heavily on time baselines between two epochs of observations and positional uncertainty (M. Narang 2022) of the survey, making it biased toward high-proper-motion stars or limited to small-volume searches. To obtain a statistical sample of radio stars across many spectral types, we adopted a simpler version of the proper-motion search outlined in L. N. Driessen et al. (2023); we will call our method of searching “radio source identification by multiepoch association.”

If a radio component is found within the search radius of the position (epoch corrected) of an optical source, they are considered to be potentially associated with each other. If such an association can be found in more than one epoch, the association is considered unambiguous. This strategy captures the high-proper-motion sources. For low-proper-motion stars, we are relying on the fact that background artifacts are less likely to randomly chance-align with proper-motion-corrected positions of optical sources at two or more epochs. Unknown steady galactic sources could still contaminate the final sample with this strategy, and this is a limitation of the results of our crossmatch strategy for the low-proper-motion stars.

To summarize, we have crossmatched the Gaia DR3 catalog with VLASS QL1 and QL2 (different epochs) to obtain two samples that we term sample A and sample B from here onward. If a VLASS component is found within  $1''$  of the Gaia DR3 source, they are considered, tentatively, to be associated with each other. If such a match can be found in both samples A and B (two epochs), the association is considered robust with little or no ambiguity. Otherwise, the VLASS component could be a background artifact (M. Narang 2022) or a highly variable candidate radio source (L. N. Driessen et al. 2023).

### 2.1. High-proper-motion Sources

The general crossmatch strategy discussed above will fail to identify high-proper-motion radio sources ( $>0''.5 \text{ yr}^{-1}$ ) observed toward the beginning or end of an SE survey. This is because VLASS takes roughly 2 yr to map its entire footprint once and in the general crossmatch strategy we only use the mean epoch. A good example is an eruptive variable G272-61B as shown in Figure 1, which has a high proper motion of  $3''.18 \text{ yr}^{-1}$ . It was observed by VLASS in 2018 April; therefore, its epoch is 2018.37. After proper-motion correction to J2018.7 (mean of

QL1), the Gaia DR3 position is still off by  $\sim 1''.5$ . With a search radius (tolerance limit) of  $1''$ , the true optical counterpart for this radio source could not have been identified. Therefore, we have separately dealt with the high-proper-motion Gaia DR3 sources to identify any radio emission from them.

To identify the high-proper-motion radio sources, we have considered a search radius of  $11''$ , which accounts for the maximum proper motion ( $10''.39 \text{ yr}^{-1}$  for Barnard’s star<sup>6</sup>) and the VLASS astrometric offset of  $0''.5$ . For all the matches, we obtained the date of observation for each of them from the Subtitle Information Table.<sup>7</sup> Next, we performed proper-motion correction of the individual high-proper-motion Gaia DR3 sources to the exact epoch and then re-searched for any VLASS components within a  $1''$  search radius. This way we recovered six high-proper-motion sources that were not found by general crossmatching.

### 2.2. Additional Filtering of the Data

The Canadian Initiative of Radio Astronomy Data Analysis (CIRADA) has used certain flags on the data in the QL1 and QL2 catalogs to denote the quality of the data. We have used the following constraints on our sample:

1. Images in the quick-look catalog (subtiles) have overlapping patches with each other. Components<sup>8</sup> detected in these overlapping areas have been cataloged twice. CIRADA has identified these duplicates and flagged them “0” for unique components and “1” and “2” for brighter and fainter duplicate components, respectively. We only retain components with duplicate flags “0” or “1.”
2. CIRADA detects components in the images by detecting blobs (flux islands) and then fitting a Gaussian to the flux islands. They flag components where a blob has been detected but no component has been fitted as “empty flux islands.” These have been denoted in the catalog with  $S\_Code = E$ . We remove such components from our main sample of crossmatches and investigate the images individually.
3. We only retain components with quality flag  $QualFlag = (0|4)$ . This ensures that we do not have detections that have peak flux density lower than 5 times the local rms, or detected components that are sidelobe features (artifacts) of nearby bright sources.

## 3. Results

Putting constraints on the Gaia DR3 catalog (parallax precision and distance cutoff), we obtained about 16 million sources that were then crossmatched with  $\sim 3.3$  million and  $\sim 3$  million sources each in the VLASS QL1 and QL2 catalogs, respectively. The crossmatch strategies yield 564 epoch 1 and 563 epoch 2 components. Additional filtering of these samples by applying VLASS flags mentioned in Section 2.2 leaves us with 417 epoch 1 and 415 epoch 2 components in samples A and B, respectively. We then checked for common components

<sup>6</sup> Although Barnard’s star is not a known radio star, we wanted to account for all possibilities.

<sup>7</sup> Refer to VLASS Quick Look and Single Epoch Catalogs web page for details on each VLASS catalog.

<sup>8</sup> Distinct localized regions of emissions in a radio image detected by source detection algorithms (PyBDSF for VLASS) are referred to as components.

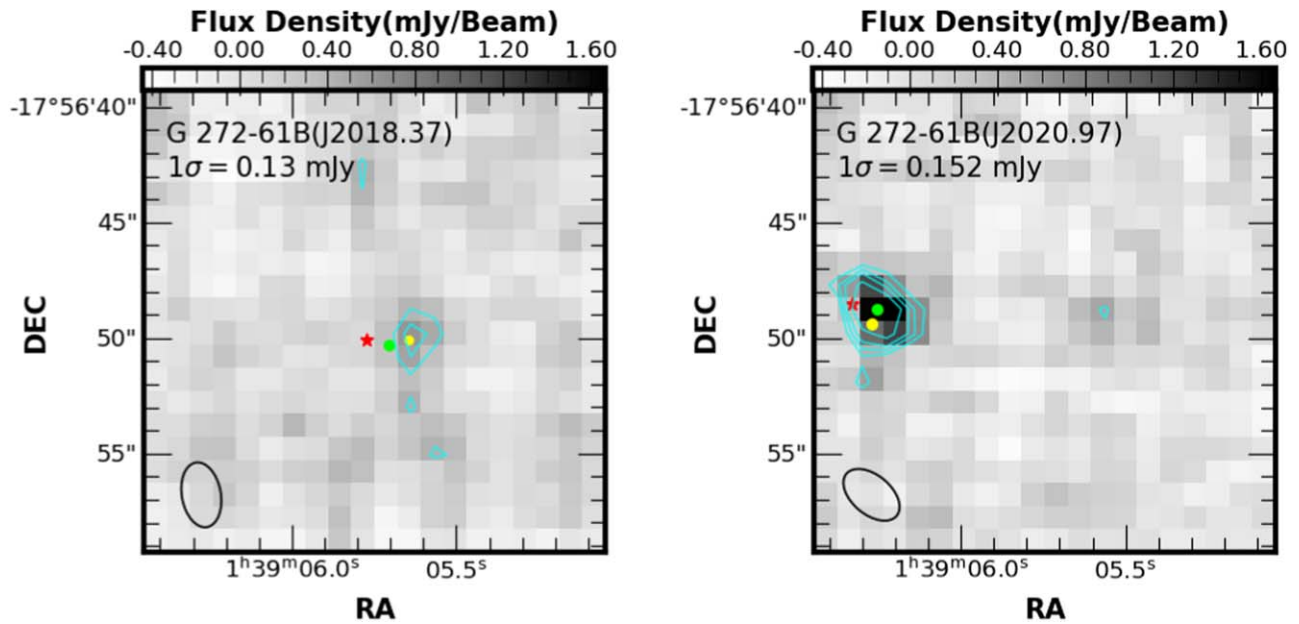


**Figure 1.** The offset between proper-motion-propagated Gaia DR3 position for the eruptive variable G272-61B and the VLASS component in epochs 1 and 2 is shown in panels (a) and (b), respectively. The red star and lime filled circle represent the Gaia DR3 position of G272-61B corrected to corresponding VLASS mean epochs and exact observed epochs, respectively. The yellow filled circle shows the VLASS 1.2 and 2.2 cataloged positions in the respective images. Contours are drawn at the  $3\sigma$ ,  $4\sigma$ ,  $5\sigma$ , and  $7\sigma$  levels, with  $\sigma$  being the local rms noise. The synthesized beam is shown as the black ellipse.

in samples A and B for robust source identification. However, upon inspecting the image tiles, we found that some of the detected components were not cataloged. The reasons for this ambiguity, as well as the methods we implemented to bypass it in order to ensure that we do not miss any sources, have been outlined in the next section.

### 3.1. Source Classification Based on Signal-to-noise Ratio and Multiepoch Detection

Crossmatching samples A and B using the Gaia DR3 ID yielded only 203 common sources. Inspecting the cutout images and image tiles using CASA (T. C. Team et al. 2022), we found an additional 190 sources detected with  $\geq 5\sigma$  radio signal in both epochs, but missing from one of the QL catalogs. These sources were found to be missing for the following reasons (as also listed in the VLASS catalog user guide):

1. Different component detection algorithms used for QL1 and QL2.
2. Excessive noise in one of the epochs, resulting in low signal-to-noise ratio (SNR) of the source. Consequently, the source was missed by the detection algorithm, or the component was flagged.
3. Detection affected by the sidelobe of a bright nearby source, hence getting flagged in one of the catalogs.

Due to equal median sensitivity in both epochs, VLASS must have observed any quiescent (steady) radio emission in both epochs. The epochs are well separated by 32 months to also be able to detect variability with large timescales. Therefore, a source detected in one of the catalogs can be missing from the other catalog because of variability or transient emission. Further, there might be some erroneous component fitting to background artifacts. We manually inspected the image tiles of all the components in samples A and B using CASA to robustly determine the steady and variable radio objects, candidate transient radio objects, and false detections.

Based on detected SNR and epoch-to-epoch variation, we could classify our sample into three types of sources:

1. sources detected in both epochs ( $\text{SNR} \geq 5\sigma$ );
2. sources detected in one epoch and only marginally detected in the other ( $4\sigma < \text{SNR} < 5\sigma$ ); and
3. sources detected only in one of the epochs, missing from the other ( $\text{SNR} < 4\sigma$ ).

The three categories have been discussed in detail in the subsequent subsections and illustrated using cutout images of three distinct types of sources as examples in Figure 2.

#### 3.1.1. Confirmed Radio Sources

The robust sample selection method outlined in previous sections returned 391 single matches and two double matches between VLASS QL1 and QL2 (both epochs) radio sources and Gaia DR3 counterparts. They were all detected in VLASS with  $\text{SNR} \geq 5\sigma$  in both epochs. We group these 393 sources into category 1, which from here onward we refer to as “confirmed radio sources.” However, due to the reasons outlined above, 203 were cataloged in both samples (thus obtained by directly crossmatching samples A and B) and 190 were identified only after further inspection of the image tiles. These 190 sources were either missing from the quick-look catalogs or flagged. We used CASA software to measure the fluxes for the missing sources and added them to the category of confirmed radio sources. The left panel of Figure 2 demonstrates an example of one such source.

#### 3.1.2. Candidate Variable Sources

Similar to confirmed sources, after crossmatching and image inspection, we could associate 14 of the radio sources with a Gaia counterpart in both epochs. However, the detections of these sources in one of the epochs are only tentative ( $4\sigma < \text{SNR} < 5\sigma$ ). We found 14 such sources and grouped

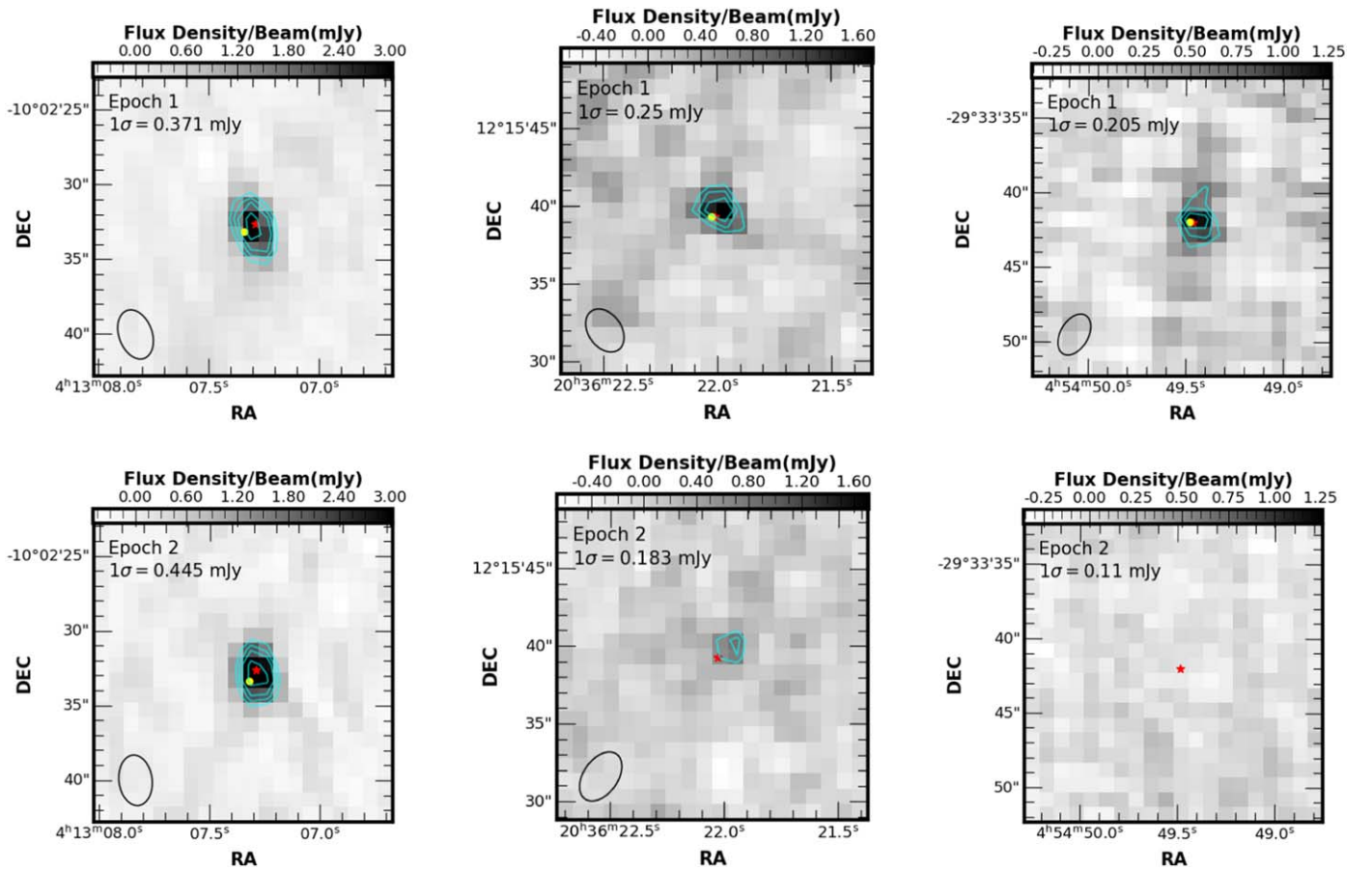


**Figure 2.** Cutouts (CIRADA cutout service) of epoch 1 (top panel) and 2 (bottom panel) observations of one source from each of the three different categories: confirmed radio sources (Gaia DR3 3192038390381997056) in the left panel, candidate radio sources (ASAS J203622+1215.3) in the middle panel, and candidate transients or highly variable sources (ST Cae) in the right panel. Contours are drawn at the  $3\sigma$ ,  $4\sigma$ ,  $5\sigma$ , and  $7\sigma$  levels, where  $\sigma$  is local rms noise. The synthesized beam at FWHM of the fitted component is shown in the lower left corner of the images. The same color scale is used for both epochs to highlight the variability in source signal and local noise. The red star shows the epoch-corrected Gaia DR3 positions, and the yellow marker shows the VLASS coordinate as reported in the QL catalog.

them into category 2, and we refer to them from here onward as “candidate variable sources.” Follow-up observations or the ongoing (at the time of writing this article) third-epoch VLASS observation is necessary to confirm emission from these candidate variable radio sources. The middle panel of Figure 2 demonstrates an example of one such candidate variable source.

### 3.1.3. Candidate Transient Objects

Significant ( $F_{\text{peak}} > 5\sigma$ ) emission in one of the epochs but no detectable emission in the other epoch can mean one of the following:

1. These are highly variable sources.
2. These are transient sources that were emitting during one of the epochs.
3. These are artifacts.

We found 191 such sources. Since we cannot confirm the nature of their emission without further observations, we grouped them into category 3 and refer to them from here onward as “candidate transients.” The right panel of Figure 2 demonstrates an example of one such “candidate transient source.”

Thus, to summarize the above results, we crossmatched samples A and B, inspected image tiles of individual components, and obtained a total of 603 VLASS sources that

have a Gaia DR3 counterpart. We found 391 confirmed radio sources, 198 candidate transients, and 14 candidate variable sources. These include a total of 11 high-proper-motion sources, six of which were not found using general crossmatch strategy. Three of them are confirmed radio sources, and three are candidate transients. Only two VLASS components got crossmatched to double Gaia DR3 sources—one of them is associated with a known spectroscopic binary (SB) system HD 239702 (A. Frasca et al. 2018), and the other component is associated with a close double. Details of all these radio sources have been provided as a machine-readable table, a part of which has been shown in Appendix B. Upon NED coordinate query, we found some sources in our sample to be of extragalactic origin. Further investigating the individual images of the remaining sources, some of them had extended double-lobed active-galactic-nucleus-like features. We discarded 24 such radio detections, which are likely of extragalactic origin or PyBDSF artifacts.

### 3.2. Source Distribution in the Sky

We have shown the sky distribution of all confirmed radio sources, candidate variable sources, and candidate transients in Figure 3. Using *Healpy*, the map was pixelated and the color map for the source density distribution was created using a 2D histogram. The map shows a distinctively dense patch of the sky of  $\approx 10^\circ \times 10^\circ$  area containing 43 sources in the southern

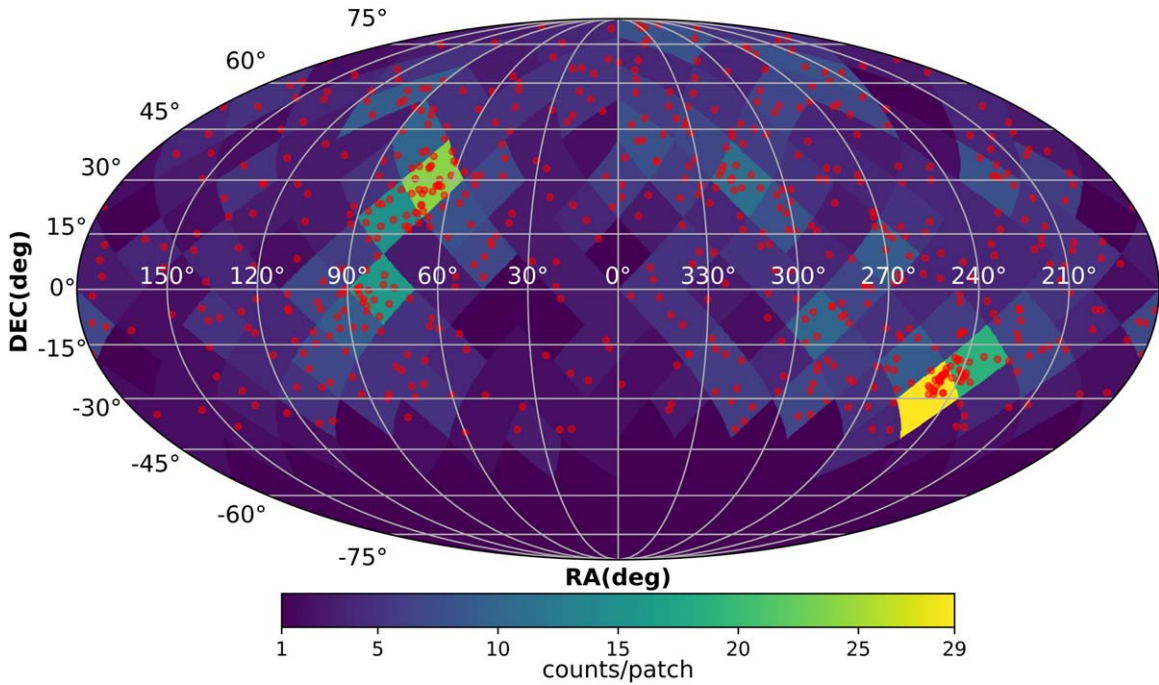


**Figure 3.** Distribution of all the confirmed and candidate sources on the sky. This color map on a Mollweide projection shows the source density per resolution, and red circles are the source coordinates.

celestial hemisphere near the Ophiuchus molecular cloud. There are two more dense regions, one in the northern sky and the other near the celestial equator containing 21 sources in the Orion Molecular Cloud. These dense patches contain confirmed and tentative detections from several YSOs, binaries, and variable objects. A serendipitous wide-field survey of these patches monitored over a long time can confirm the candidate sources and provide insights about this population of young radio stars. Figure 4 shows the distribution of distances to all 603 radio sources with Gaia DR3 counterparts.

### 3.3. Gaia Color–Magnitude Diagram

Gaia DR3 photometry provides us with apparent magnitudes. Using  $BP - RP$  and  $G_{\text{mag}}$  from the Gaia DR3 catalog and the MS cutoff from B. Banerjee et al. (2024) and Narang et al. (in preparation) based on the MS color–magnitude relation from M. J. Pecaut & E. E. Mamajek (2013),<sup>9</sup> we categorized the 3 GHz radio sources that we obtained from the VLASS-Gaia DR3 crossmatch into different spectral types. To separate the MS objects in the color–magnitude diagram (CMD), we implemented the following equation:

$$M_G = -0.43(BP - RP)^2 + 4.72(BP - RP) + 1. \quad (1)$$

Figure 5 shows the CMD for our entire sample. To highlight the contrast in the population of radio sources against the optical sources, we have plotted the VLASS sources in the foreground of the Gaia DR3 sources (yellow).

### 3.4. Distinct Populations of Radio Emitters

Prior knowledge of the object type combined can provide us with insights into the physical processes driving the radio emission in these sources. Following H. K. Vedantham et al. (2022) and T. W. H. Yiu et al. (2024), we used data from

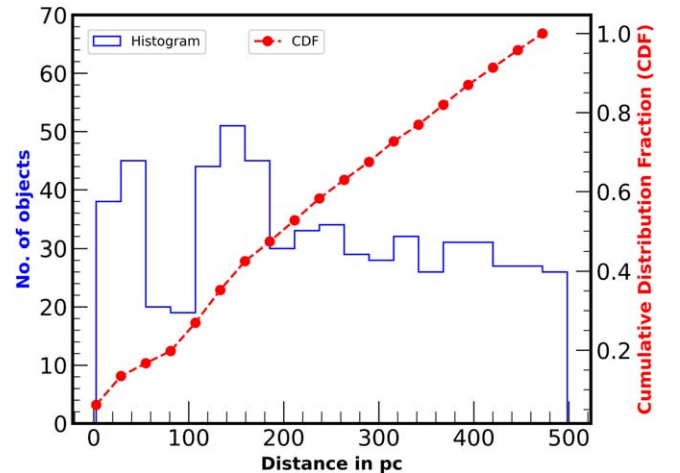


**Figure 4.** Distance distribution of the entire sample. The solid blue line represents the distribution of distances to all the sources. The cumulative distribution function is shown in red.

SIMBAD (M. Wenger et al. 2000) to classify the object type for the detected sources. Among the 391 confirmed radio sources, we could only find 207 sources in SIMBAD. Figure 6 shows the Gaia CMD for the SIMBAD-identified confirmed radio sources.

From Figures 5 and 6, we can already infer some of the demographic features:

1. About 4% of the 603 sources (i.e., 23) in our entire sample are B-, A-, and early F-type radio stars.
2. Roughly 48% of the radio sources lie above the MS. These sources are mostly binaries and YSOs as seen in Figure 6. These sources are highly variable radio sources. Many of them are candidate variables and candidate transients.

<sup>9</sup> Updated Table based on Pecaut and Mamajek 2013

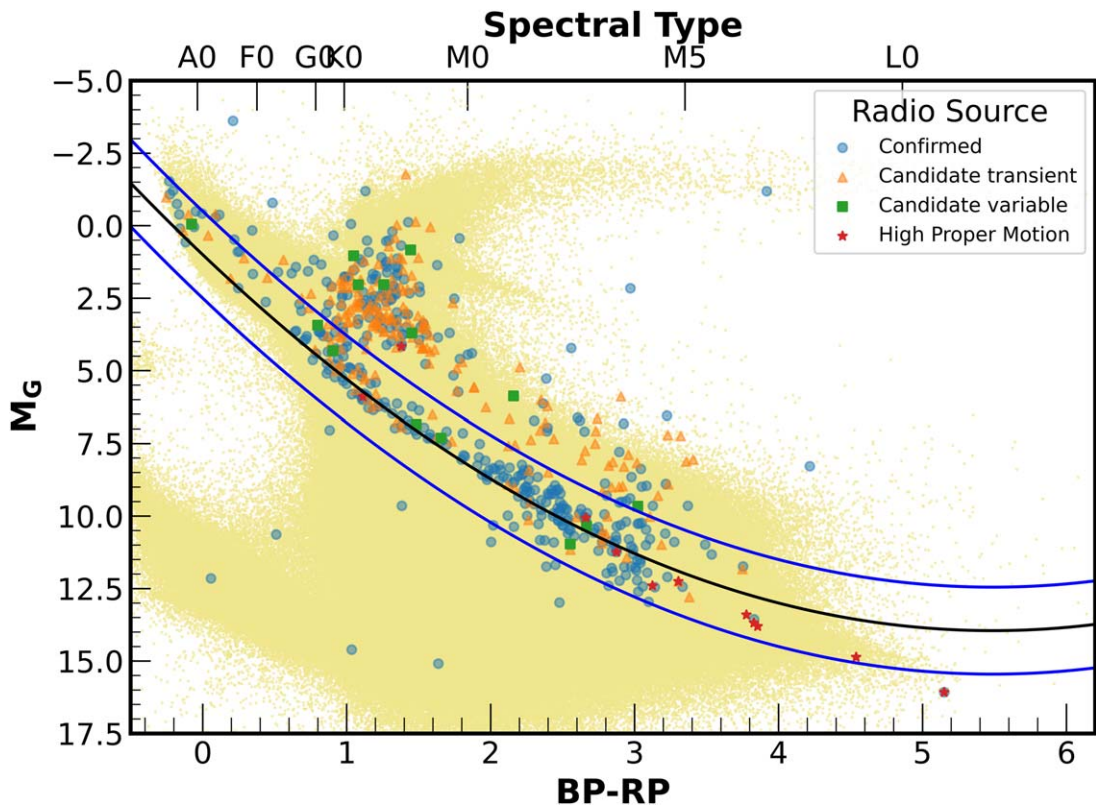


**Figure 5.** The yellow scatter plot in the background shows all the Gaia DR3 optical sources within 500 pc. The foreground scatter plot is for 3 GHz sources in our total sample. The three categories and stars with high proper motion ( $PM > 0''.5 \text{ yr}^{-1}$ ) are shown with different markers. The black line corresponds to a fit for the MS sources in the CMD (Equation (1)). The blue lines represent the tolerance on  $M_G = \pm 1.5$  for the MS sources.

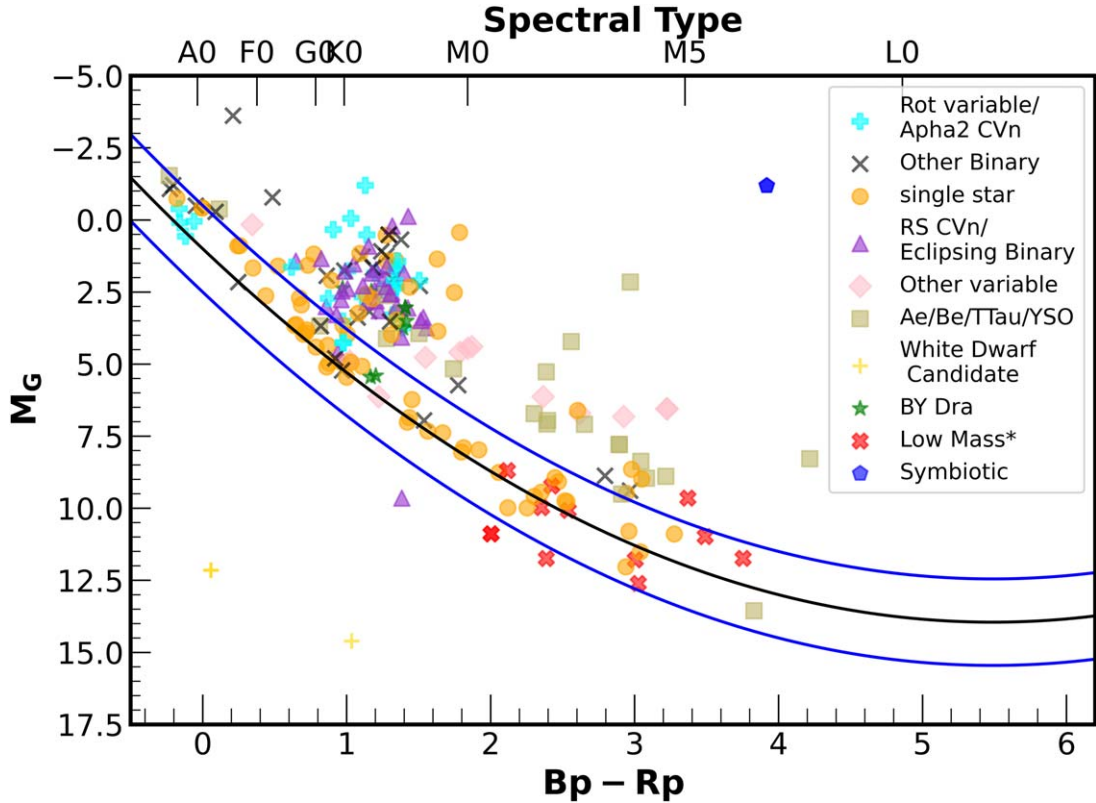


**Figure 6.** The Gaia CMD for 207 of the 391 confirmed radio sources that were also found in SIMBAD by a  $2''.5$ -radius query. Different object types have been represented using different shapes.

3. Late F- to early M-type typical radio stars constitute  $\approx 27\%$  of our sample. They are mostly single stars and are expected to emit in radio because of chromospheric activity.
4. Late M dwarf types constitute  $\approx 19\%$  of our sample despite the fact that they do not possess magnetic dynamos. Studying radio emission from ultracool dwarfs will help us bridge the gap in our understanding of the origin of stellar and planetary magnetic fields.
5. Two out of the 203 SIMBAD-identified sources in our sample are white dwarf candidates.

In Section 4, we discuss how various properties of radio emission vary across spectral types and object types. Some of the known radio emitters from these SIMBAD-identified object types have been discussed in Appendix A.

#### 4. Discussion

By studying the nature of radio emission, we can estimate the region of origin (photosphere, chromosphere, corona, wind, etc.) and the physical processes driving the emission (photospheric magnetic fields, chromospheric activity, coronal ejections, magnetically trapped winds, etc.), which provides insights into the stellar structure and ambient conditions. We discuss the radio brightness temperature, radio variability, and correlation between radio and X-ray flux for our sample and how they vary across different spectral and object types. In-band spectral index calculations are performed using SE images, which can be found in the SE catalogs. However, they are partially incomplete; therefore, we do not analyze spectral index variation in our study.

##### 4.1. Brightness Temperatures

The temperature of a blackbody having the same observed radio brightness (specific intensity,  $I_\nu$ ) at a frequency  $\nu$  as observed in a source is referred to as the brightness temperature ( $T_b$ ) for that source at  $\nu$ . Brightness temperature is a proxy for the emission mechanism (coherent or incoherent; bremsstrahlung, gyrosynchrotron, Electron Cyclotron Maser Instability (ECMI), etc.; M. Gudel 2002). Since the continuum at radio frequencies can be described by the Rayleigh–Jeans law, specific intensity  $I_\nu$  is given as

$$I_\nu = \frac{2kT_b\nu^2}{c^2},$$

where  $k$  is Boltzmann’s constant and  $c$  is the speed of light. The observed flux density  $S_\nu = I_\nu A/d^2$ , where  $A$  is the cross-sectional area of the source perpendicular to the line of sight and  $d$  is the distance to the source. Now we can write the brightness temperature as (M. Gudel 2002)

$$T_b = \frac{S_\nu d^2 c^2}{2Ak\nu^2} \sim \left( \frac{S_\nu}{1 \text{ mJy}} \right) \left( \frac{d}{1 \text{ pc}} \right)^2 \left( \frac{10^{11} \text{ cm}^2}{r^2} \right) \left( \frac{1 \text{ GHz}}{\nu} \right)^2 10^7 \text{ K}, \quad (2)$$

where we assume a perfectly spherical source region of radius  $r$ . For our sample,  $\nu = 3 \text{ GHz}$  and  $S_{3 \text{ GHz}}$  is the peak flux density ( $F_{\text{peak}}$ ) as provided by the quick-look catalog or inferred using CASA (for components that were not cataloged). The QL catalogs provide the deconvolved beam size and peak

and integrated flux densities. Since we are dealing with point sources, we consider the listed peak flux density per beam for the analysis. We calculated brightness temperatures for sources whose stellar radius  $r$  is obtained from the Gaia DR3 catalog for astrophysical parameters (Gaia Collaboration et al. 2023). These radius estimates are based on the General Stellar Parameterizer using Photometry (GSP-Phot), which uses certain forward-modeling approaches as explained in R. Andrae et al. 2023.

##### 4.2. Emission Mechanism

VCLASS is not sensitive enough to detect photospheric continuum radio emission. The hottest star in our sample is a B8V type. It has to be within 6 pc for its continuum radio emission to be detected by VCLASS, whose rms sensitivity is  $\approx 120 \mu\text{Jy}$ . The only radio source in our sample within 6 pc is the M6V-type flaring dwarf WX UMa, which has too cool of a photosphere to be detected by VCLASS. This ensures that emission from all objects in our sample is of nonphotospheric origin.

Other types of emission mechanisms, both thermal and nonthermal, are produced by highly energetic charged particles. Emission mechanisms can be characterized roughly based on brightness temperatures (as described in the review by M. Gudel 2002):

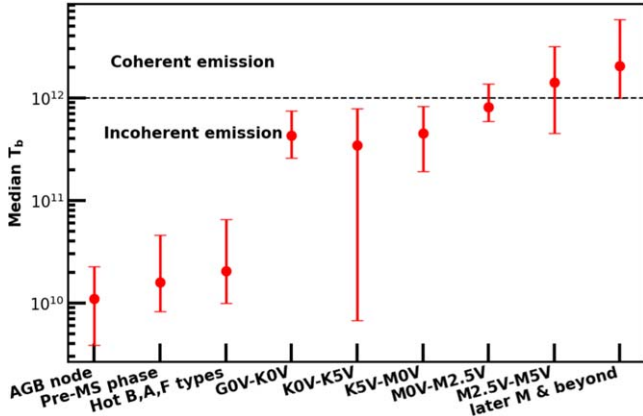
1. *Bremsstrahlung radiation* originates from thermal or relativistic plasma. These emission mechanisms are limited up to  $T_b \approx 10^6 \text{ K}$ .
2. *Cyclotron radiation* can result from magnetized thermal plasma. These mechanisms are limited up to  $T_b \approx 10^8 \text{ K}$ .
3. *Gyrosynchrotron emission* can occur owing to mildly relativistic thermal and power-law electron distributions. These mechanisms can explain  $T_b$  up to  $\approx 10^9 \text{ K}$ .
4. *Synchrotron radiation* can be caused only by relativistic power-law electron distribution. These mechanisms are highly polarized and can go as high as  $T_b \approx 10^{12} \text{ K}$ .
5. *Coherent plasma radiation* is also highly polarized and can explain emissions with  $10^{12} \text{ K} < T_b < 10^{16} \text{ K}$ .
6. *Electron cyclotron maser* accounts for any emission with  $T_b > 10^{16} \text{ K}$ . These emissions are almost completely polarized radiation.

Figure 7 shows the median of brightness temperatures calculated using Equation (2) of different populations of radio sources in our sample as identified from the Gaia CMD.

There is a known underestimation of 8%–15% in the peak flux measurements as reported by CIRADA in the QL1 catalog. Further, the radius of the stars provided in Gaia DR3 can give the best estimate of  $T_b$  only if the emission is of chromospheric origin (assuming that the radius of a chromosphere is similar to the photosphere). It would, however, underestimate  $T_b$  if the emission is a collimated beam from a smaller patch of the star ( $r_{\text{source}} < r$ ). It would overestimate  $T_b$  if the emission is from the entire corona, disk, or wind, which has  $r_{\text{source}} \gg r$ . Therefore, our calculated  $T_b$  of individual objects alone cannot provide us with the most precise picture of the actual origin of their radio emissions. Nevertheless, from Figure 7 we can draw a general trend in the brightness temperatures of different object types and make general inferences, which can be tested with follow-up observations.

From Figure 7, we observe the following:





**Figure 7.** Median brightness temperatures at 3 GHz of giant, pre-MS, and different MS spectral types. Quartiles 1 and 3 have been shown using error bars that represent the central scatter around the median. Coherent and incoherent emissions can be distinguished by the  $T_b = 10^{12}$  K (M. Gudel 2002) line.

1. Incoherent gyrosynchrotron emission ( $T_b < 10^{12}$  K) mechanisms dominate in the objects above MS and hot B-, A-, and F-type stars.
2. G- and K-type stars are mostly incoherent gyrosynchrotron emitters with relativistic power-law electron distributions (M. Gudel 2002).
3. In later K-type and early M-type stars, relativistic synchrotron emission from plasma bursts and flares dominate the radio emission (J. R. Callingham et al. 2021; T. W. H. Yiu et al. 2024).
4. MS stars show a general trend of increasing brightness temperatures for cooler stars, along with a transition in the emission mechanism from incoherent to coherent around mid-M type (see Figure 7).

Although our analysis indicates a trend of incoherent emissions from B- and A-type stars because of larger photospheric radius, multifrequency radio observations of hot stars have revealed highly polarized ECM emission beamed from smaller source regions (e.g., B. Das et al. 2020, 2022). Therefore, observed B- and A-type stars need to be followed up at other frequencies to unambiguously interpret their radio emission. We also have four MS F0- to F6-type stars in our sample. Since early F-type stars have shallow convective zones and weak stellar wind, we do not expect them to be able to power detectable radio emissions. Therefore, further follow-up on these F-type stars can reveal new insights into stellar structure (D. Ayanabha et al. 2024, in preparation).

Cooler dwarfs (later than M2.5V types) are found to exhibit high brightness temperatures ( $T_b > 10^{12}$  K), indicating that coherent emissions are ubiquitous in ultracool and brown dwarfs. This spectral range corresponds to the transition from partial to fully convective interiors (A. Reiners & G. Basri 2009; I. Baraffe & G. Chabrier 2018; W.-C. Jao et al. 2018). With the lack of a tachocline, magnetic fields in these types of objects are thought to originate from mechanisms different from solar dynamos (M. Kao et al. 2017; T. W. H. Yiu et al. 2024), which possibly power the observed radio emission. If these dwarfs possess weaker magnetic fields, they might emit mostly at much lower frequencies. We should be able to observe faint decimetric emission and bright emission at low frequencies (J. R. Callingham et al. 2021; T. W. H. Yiu et al. 2024) from these dwarfs. Low-frequency observations are

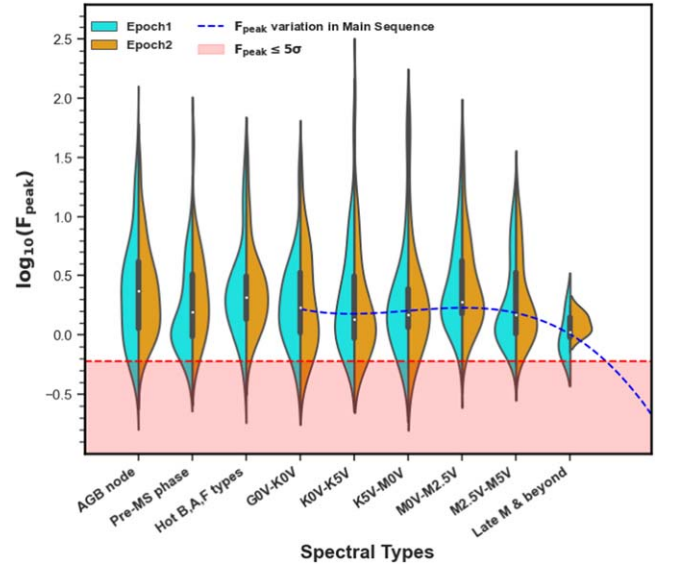


**Figure 8.** Variation of peak flux density with spectral types. White points and bold boxes inside the violins show the median and interquartile range, while the violin edges represent the distribution. SE VLASS images are mostly sensitive to the area above the shaded region ( $F_{\text{peak}} > 5\sigma$ ). The blue dashed line shows extrapolated median flux variation for late M types.

crucial to completely understand the nature of these radio-emitting dwarfs (B. Burningham et al. 2016; M. Narang et al. 2024, in preparation). The dearth of detection of late M types and cooler dwarfs in our sample is because they are faint emitters at 3 GHz and VLASS SE quick-look images do not have the required sensitivity to detect them.

Figure 8 shows that observed median flux densities drop off for cooler dwarfs. Emission from these dwarfs is possibly due to ECMI that is beamed from small patches (H. K. Vedantam 2020; S. E. B. Toet et al. 2021), resulting in the net radio output being relatively low. Deeper observations with higher SNR or even the three-epoch-stacked deep-cleaned VLASS images are likely to reveal more cool dwarfs emitting in 3 GHz.

### 4.3. Radio Variability of 3 GHz Emitters

Nonthermal radio emissions are generally variable, whereas thermal emissions are quiescent (e.g., M. Gudel 2002). We have used the two-epoch flux measurements for confirmed sources to report a general trend of variability for our sample. We have used the quantity  $\beta = \Delta F_{\text{peak}}/F_{\text{av}}$  to quantify the extent of variability as visualized in Figure 9.  $\Delta F_{\text{peak}} = |F_1 - F_2|$  is the change in peak flux measured between two epochs, and  $F_{\text{av}} = (F_1 + F_2)/2$  is the mean peak flux. Any source with  $\beta > 0.2$  should be considered to be significantly variable (between the two epochs). Otherwise, the radio emission can be<sup>10</sup> considered to be quiescent.

It is to be noted, however, that two epochs of observations are not sufficient to provide a true measure of the amplitude and timescale of the variability. VLASS epoch 3 data release and individual follow-ups are necessary for properly characterizing short-term and even long-term variability.

<sup>10</sup> Short-term variability caused by flares or periodic variation triggered by SPIs can be missed by on-the-fly short-integration VLASS observations.

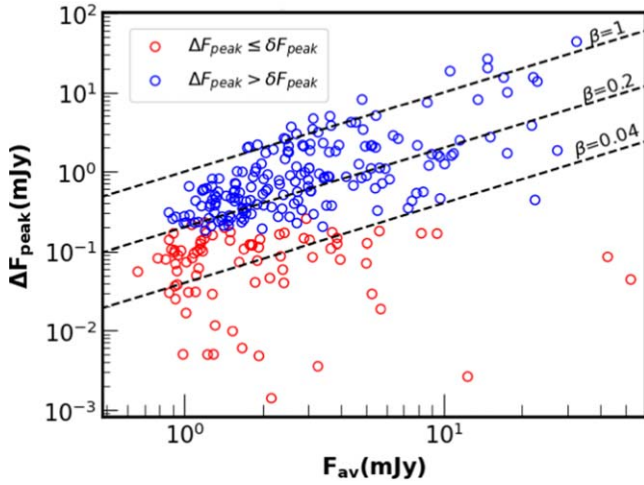


**Figure 9.** Sources varying by more than the uncertainty in flux measurement ( $\delta F_{\text{peak}} = \sqrt{\delta F_1^2 + \delta F_2^2}$ ) are denoted by blue; otherwise, by red. The dashed lines indicate different values of  $\beta$ .

#### 4.4. Correlation between Radio and X-Ray Output

Flares in stars are generated when energetic plasma trapped in magnetic loops is released. Most of the energy in the magnetic fields is emitted in low-frequency X-rays through thermal bremsstrahlung radiation and is thought to be responsible for coronal heating while a fraction of the energy accelerates the trapped plasma (A. O. Benz & M. Güdel 2010). This nonthermal power-law plasma emits gyrosynchrotron radio emission. Therefore, we expect a correlation between observed radio and soft X-ray emissions from magnetic plasma environments present in stellar atmospheres (M. Güdel et al. 1993; A. O. Benz & M. Güdel 1994). Such a correlation is indicative of the contribution of flares in heating of the stellar corona and the efficiency with which flares accelerate the plasma. On the other hand, neutral atmospheres in cooler dwarfs are quieter in X-ray but can still be radio bright. They are expected to deviate from such a radio–X-ray correlation (B. Burningham et al. 2016; H. K. Vedantham et al. 2022).

We crossmatched our sample of confirmed radio sources with the XMM-Newton Serendipitous Survey Catalog (N. A. Webb et al. 2020, 2023) to obtain 44 matches. Their X-ray (0.2–12 keV) and radio (2–4 GHz) luminosities (derived from average peak flux density measurement) have been plotted in Figure 10.

To test the correlation between radio and X-ray log luminosity, we opted for the Pearson- $\rho$  test rather than a rank correlation test since we do not have a very large number of rank ties. The Pearson test gives  $\rho = 0.5$  with a  $p$ -value of  $5.3 \times 10^{-4}$ , indicating a positive correlation with moderately significant confidence. For the entire matched sample, we find a best-fit correlation as

$$L_X = 10^{19.97 \pm 2.75} L_{3\text{GHz}}^{0.63 \pm 0.16}. \quad (3)$$

Follow-up near-simultaneous observations at X-ray and radio wavelengths of these types of sources are crucial to precisely study this correlation.

This correlation relates stellar chromospheric activity to the heating of stellar coronae, which is not very well understood. In addition, these data corroborate the mounting evidence of the fact that flares are not uncommon in YSOs. Understanding their

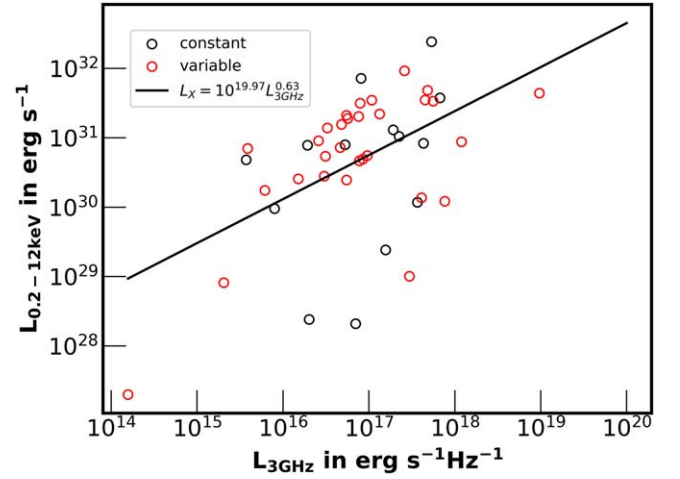


**Figure 10.** Variable ( $\beta > 0.2$ ) and quiescent ( $\beta < 0.2$ ) sources are denoted by red and black circles, respectively. The black line is a linear fit.

origin is key to understanding the origin of stellar magnetic fields and the loss of fossil fields.

## 5. Summary

In this work we carried out a systemic analysis of the VLASS epoch 1 and 2 data, in combination with Gaia DR3, to investigate the population of radio stars within 500 pc. VLASS QL1 and QL2 catalogs were crossmatched with Gaia DR3 to identify 3 GHz radio stellar sources within 500 pc. To reduce chance coincidence with background artifacts and galaxies and to ensure that we do not miss any radio source as a result of inaccuracy in source detection algorithm, we implemented robust crossmatching techniques and inspected individual image tiles. Below, we summarize the major results from our demographic analysis of a homogeneous radio stellar population that we produced.

1. Epoch 1 detections were compared with epoch 2 detections to classify the radio sources into three categories:
  - (a) *Confirmed radio sources.* They were detected in both epochs with  $\geq 5\sigma$  signal.
  - (b) *Candidate variable sources.* They were detected in one epoch with  $\geq 5\sigma$  signal but only tentatively ( $4\sigma < \text{SNR} < 5\sigma$ ) in the other epoch.
  - (c) *Candidate transient sources.* They were detected with  $\geq 5\sigma$  signal in one epoch but no detection in the other.
2. Based on the Gaia CMD, we find that most of our sample consists of both single and binary F-, G-, K-, and M-type MS stars. We also report a few atypical B-, A-, and early F-type radio stars and white dwarf candidates.
3. Apart from MS stars, we also find a large population of YSOs and moving group members.
4. We analyze the radio brightness temperature of the sources to infer qualitatively the type of mechanism that drives radio emission in a star of a particular spectral and object type. We find that M dwarfs mostly exhibit coherent radio emission whereas most other stars are typically incoherent radio emitters.
5. We crossmatched our sample with the XMM-Newton Serendipitous Survey catalog to test for any relation between radio and X-ray flux. We find a moderately significant positive correlation,  $L_X \propto L_{3\text{GHz}}^{0.63 \pm 0.16}$ .

The results from this study and our sample of radio-bright stars within 500 pc can serve not only as a valuable resource for understanding the radio emission from stars but also as a robust sample for further follow-up studies.

### Acknowledgments

We thank the reviewer for their constructive comments, which helped to improve the clarity and sharpness of the presentation. This research has made use of the SIMBAD database, operated at CDS, Strasbourg, France. The National Radio Astronomy Observatory is a facility of the National Science Foundation operated under a cooperative agreement by Associated Universities, Inc. CIRADA is funded by a grant from the Canada Foundation for Innovation 2017 Innovation Fund (Project 35999), as well as by the provinces of Ontario, British Columbia, Alberta, Manitoba, and Quebec. This work presents results from the European Space Agency (ESA) space mission Gaia. Gaia data are being processed by the Gaia Data Processing and Analysis Consortium (DPAC). Funding for the DPAC is provided by national institutions, in particular the institutions participating in the Gaia MultiLateral Agreement (MLA). The Gaia mission website is <https://www.cosmos.esa.int/gaia>. The Gaia archive website is <https://archives.esac.esa.int/gaia>. This study has made use of data obtained from the 4XMM XMM-Newton serendipitous source catalog compiled by the XMM-Newton Survey Science Centre Consortium. A.D. would like to thank the Department of Astronomy and Astrophysics (DAA) at TIFR for hosting them during the course of this research. The support and resources provided by TIFR were invaluable to the completion of this work. P.K.N. acknowledges support from the Centro de Astrofísica y Tecnologías Afines (CATA) fellowship via grant Agencia Nacional de Investigación y Desarrollo (ANID), BASAL FB210003.

### Appendix A Source Description

Below we briefly discuss some of the sources whose spectral type and evolutionary stages are robustly determined. The SIMBAD identifier of these sources has been highlighted by bold text.

#### A.1. Hot B, A, and Early F-type Stars

OB-type stars are rare in the solar neighborhood as evident in the background Gaia DR3 source plot in Figure 5. Despite the lack of convective layers, due to their radiative outer layers, they have ionized winds, and some retain strong fossil fields (J. F. Donati & J. D. Landstreet 2009). Gyrosynchrotron emission and synchrotron emission have been observed from optical thick coronae, or winds of these stars, or colliding wind of contact binaries (M. Güdel 2002). Since we have a large volume-limited sample, we do find some late B-type stars in addition to a few A- and early F-type stars. We confirm steady radio emission from chemically peculiar Be star HD 23478 and single MCP star HD 182180. One of the candidate variable sources, HD 34736, has a strong magnetic field and is suspected to be an interacting close binary system (E. A. Semenko et al. 2014). Young B-type star  $\sigma$  Ori E (part of open star cluster  $\sigma$  Orionis) shows variable peak radio flux. It is spinning down owing to magnetic braking (R. H. D. Townsend et al. 2013). This star can provide a peek into the early evolution of

stellar structure and magnetic fields. Further, we confirm steady emission from three  $\alpha^2$  Canum Venaticorum ( $\alpha^2$  CVn) variable stars, two rotational variable stars, and a double-star system.

Bright X-ray source (F. M. Walter et al. 2003) HD 28867 exhibits variable radio emission. It is a B9V YSO in the Taurus–Auriga star-forming region. Known Algol-type eclipsing binary RZ Cas shows high variability. We further report confirmed and potential transient detections from three more eclipsing binaries, one double star, two pulsating variables, and six single stars. Likely because of companions, the absolute magnitude and color indices change, shifting them above the MS. The confirmed variable source TYC 5366-707-1 might be an MCP MS F-type star.

#### A.2. RS CVn, Spectroscopic, and Eclipsing Binaries

Binaries and visual doubles with MS components deviate from the MS (beyond blue lines in Figure 5), due to extra measured luminosity added by their companions. We find 30 confirmed, 18 candidate transient, and 1 candidate variable emission from RS CVn binaries. They mostly populate the region above MS ranging from F to M types. The late-type stars in these systems possess strong magnetic fields, resulting in gyrosynchrotron emission (D. H. Morris & R. L. Mutel 1988) and heightened chromospheric activity due to interacting magnetic fields causing synchrotron or coherent ECMI polarized emission. Though the former is detectable in decimetric bands, the latter is detectable at much lower frequencies (S. E. B. Toet et al. 2021) not covered by VLASS. These systems show very high variability. DM UMa dims by over an order of magnitude<sup>11</sup> from epoch 1 to epoch 2. They are bright X-ray sources and show strong Ca II triplet and H $\alpha$  absorption features, which are other chromospheric activity indicators (L. Zhang et al. 2016).

Eight detections were made from close doubles (or visual binaries). High-proper-motion sources  $\alpha$  For A and B are visually separated by 5". Using a proper-motion search and a 1" search radius, we can confidently associate the radio emission with the X-ray source  $\alpha$  For B. A total of 15 confirmed, 1 candidate variable, and 10 candidate transient SBs were found. A total of 6 confirmed, 1 candidate variable, and 11 candidate transient sources were associated with eclipsing binaries. Colliding winds and mass transfer can accelerate charges and drive radio emissions in these binaries.

#### A.3. BY Dra, Eruptive, and $\alpha^2$ CVn Variables

BY Draconis–type variables (BY Dra variables) are chromospheric variables with inhomogeneous photospheric features caused by strong persistent magnetic fields. They can be fast-rotating young stars like BO Mic or late-type dwarfs like V402 Hya. Seven confirmed, eight candidate transients, and one candidate variable BY Dra sources were found. They populate a large fraction of the region above the MS. The rest is composed of  $\alpha^2$  CVn, pulsating and eruptive variables, and YSOs. We find five pulsating variable stars in our total sample, out of which only HD 218779 is associated with confirmed radio detection and the other four were only detected in one of the epochs. The eruptive variable 2MASS J21103096–2710513 is an optical flaring M dwarf (L. Doyle et al. 2019) that shows potential transient 3 GHz emission.

<sup>11</sup> By the extent of variability, we mean the range of measured 3 GHz flux. The variability timescales can be much shorter than 32 months.

#### A.4. Young Stellar Objects

We also find a large number of pre-MS objects in our radio sample. Due to strong magnetic fields, magnetic braking, accretion, and persistent flaring activity are ubiquitous in protostars. HD 200391 and EM\* MWC 297 are two Herbig Ae/Be stars that exhibit steady and variable emission, respectively. There are 10 YSO candidates, 6 confirmed detections, and 4 potential transient emissions from known YSOs. T Tauri stars are highly common in our sample. A total of 8 confirmed detections, 1 candidate variable, and 15 candidate transient emissions from T Tauri stars have been found. T Tau is found in our sample with variable brightness. Variable 5 GHz emission from candidate transient source V1201 Tau had been observed using very long baseline interferometry by P. A. B. Galli et al. (2018).

#### A.5. Partially Convective Stars (F3V–M2.5V MS Stars)

Stars in the mass range  $0.4M_{\odot} \lesssim M_{*} \lesssim 1.45M_{\odot}$  have radiative cores and outer convective layers. Differential rotation in the convective zone beginning at the tachocline (the boundary between the radiative and convective zone) generates the magnetic field in these stars. Shear and turbulence in the field lines caused by differential rotation drive persistent magnetic activities. V815 Her is a steady emitter in our sample that demonstrates Sun-like magnetic fields (Z. Kovari et al. 2024). Steady gyrosynchrotron emission caused by solar-type microflares, variable emission of short timescales caused by solar-type bursts, and optically thick bremsstrahlung radiation from solar like coronae have been commonly observed. Coherent emission due to magneto-ionic plasma oscillations is ubiquitous in these magnetic stars.

The 12 candidate transient and 2 candidate variable sources in this range are binaries, variable stars, and T Tauris stars. The 47 confirmed detections are mostly from isolated single stars and a few variables and binaries. As expected, these confirmed sources mostly show quiescent emission. Only three are significantly variable, while a few are only mildly variable.

#### A.6. Fully Convective Stars and Ultracool Dwarfs

M2.5V and later-type dwarfs ( $M_{*} \gtrsim 0.4M_{\odot}$ ) have completely convective interiors with no tachocline. We do not have any clue whether such stars can generate magnetic fields of their own. Even if they retain fossil fields, they are slow rotors and would not be able to generate as much activity. However, we find roughly 19% of our entire sample to be late M dwarfs,

four of which are ultracool dwarfs (later than M6V type) exhibiting emission with high brightness temperatures. Coherent plasma emission or ECMI can be a result of Jupiter-like large-scale magnetospheric dynamics (T. W. H. Yiu et al. 2024).

Eruptive high-proper-motion M6 dwarfs WX UMa and G272-61B were seen to significantly vary over two epochs, meaning that they might have been caught flaring in one of the epochs. We performed a crossmatch of the total sample with the latest ultracool dwarf catalog (W. M. J. Best 2020) to find two crossmatches. We associate the M8.5V-type dwarf LSR J1835+3259 with a confirmed radio source and M7V-type dwarf LSR J0510+2713 with a candidate variable source.

#### A.7. Below Main Sequence

Two confirmed emissions are from candidate white dwarfs. They show highly variable emissions. Terrestrial planets orbiting close to a white dwarf can induce ECMI emissions (A. J. Willes & K. Wu 2005). Eclipsing binary system AR Scorpii, consisting of a red and a white dwarf, exhibits highly variable emission. Episodic mass transfer between the dwarfs can be a reason for strong X-ray and radio emission. Further, two low-mass single confirmed radio stars were found below the MS. The reason for their deviation from the MS is unknown.

#### A.8. Planet-hosting Radio Systems and SPI

The NASA Exoplanet Archive (NEA) catalog, containing composite data for all the confirmed planets, was crossmatched with our sample to search for any 3 GHz planet-hosting radio source. We did not find any match results. On crossmatching with TESS and Kepler candidates, we obtained a null result. However, a K2 false positive, EPIC 204165788.01, crossmatched with our sample. It turns out that it is most likely an eclipsing binary companion (A. C. Rizzuto et al. 2017) to the primary source HIP 80474.

### Appendix B Source Information Table




A table containing the important crossmatching information for our entire sample of radio sources can be found in the machine-readable format that is provided as a supplement to this article. Table 1 is an example table for our entire sample containing 20 rows with SIMBAD identifiers and object types.

**Table 1**  
VLASS, Gaia DR3 Coordinates, and Photometric Information for Radio Sources Analyzed in this Study along with Their Classified Category

Gaia DR3 ID	RAJ2000 (deg)	DEJ2000 (deg)	RAJ2016 (deg)	DEJ2016 (deg)	Gmag	BP-RP	Distance (pc)	$F_1$ (mJy beam <sup>-1</sup> )	$F_2$ (mJy beam <sup>-1</sup> )	SIMBAD ID	Object Type	Category
2137474969751117312	295.961235	53.628456	295.961257	53.628387	15.56	2.77	97.60	1.02	1.05	...	...	Confirmed
6123452251070601216	215.462699	-32.529573	215.462559	-32.529713	17.43	3.01	129.21	1.84	1.50	...	...	Confirmed
3263936692671872512	54.196898	0.587005	54.196900	0.587042	5.61	1.24	29.43	14.42	29.89	...	...	Confirmed
852710613536664320	151.387383	54.869795	151.387126	54.869893	15.98	2.03	328.36	1.12	1.09	...	...	Confirmed
837388987723516160	162.460460	52.145103	162.460313	52.145178	14.59	1.34	333.83	0.86	0.97	2MASS J10495046 +5208426	QSO_Candidate	Confirmed
3120983344792501760	98.146173	2.125023	98.146211	2.125139	17.71	3.08	219.15	9.49	9.33	...	...	Confirmed
4358897712402949632	246.359619	-1.514793	246.359654	-1.514962	19.38	3.02	271.37	3.34	2.77	...	...	Confirmed
3425077749587261440	92.366361	22.607323	92.366431	22.607449	9.48	0.98	110.87	1.10	1.20	HD 252406	RotV*	Confirmed
2149628932626002432	271.589520	53.706824	271.589599	53.706930	19.15	3.33	219.77	1.30	1.32	...	...	Confirmed
2081589817375031552	303.704521	45.028497	303.704452	45.028526	7.43	1.29	242.18	4.92	12.33	HD 192785	SB*	Confirmed
1847913321237991168	318.557265	27.130139	318.557201	27.130327	18.55	2.93	228.92	1.85	1.89	...	...	Confirmed
6237015550067391488	238.482658	-23.978140	238.482701	-23.978203	5.36	0	143.06	26.48	28.33	PMN J1553-2358	Radio	Confirmed
1282848220976683264	220.644340	30.475647	220.644200	30.475568	13.66	1.42	213.28	0.84	0.94	FIRST J144234.6 +302832	Radio	Confirmed
3314244361868724224	68.387867	18.016700	68.387760	18.016635	6.89	0.26	157.97	1.36	1.90	HD 28867A	Star	Confirmed
213484274324058624	81.250454	49.317162	81.250313	49.317184	10.47	1.32	273.44	3.00	2.11	BD+49 1348	RotV*	Confirmed
861644351670829440	163.930856	60.469315	163.931091	60.469333	8.91	1.3	185.66	27.92	1.59	V* DM UMa	RSCVnV*	Confirmed
663853582908635520	126.572705	20.577804	126.572567	20.577690	15.35	1.81	309.44	2.45	2.84	2MASS J08261745 +2034402	Star	Confirmed
6235747125966268416	238.664660	-25.243768	238.664642	-25.243848	5.84	-0.06	144.23	2.60	2.82	* 3 Sco	RotV*	Confirmed
2694353690543010304	324.417830	1.620317	324.417836	1.620191	12.16	2.97	35.91	1.38	1.83	RX J2137.6+0137	**	Confirmed
1005873614080407168	91.375387	60.818969	91.375153	60.819401	12.30	2.87	16.28	8.13	2.15	...	...	Confirmed
1328866562170960384	243.668683	33.858221	243.668787	33.858226	5.43	0.81	22.70	3.19	6.56	...	...	Confirmed

(This table is available in its entirety in machine-readable form in the [online article](#).)

## ORCID iDs

D. Ayanabha  <https://orcid.org/0000-0001-8845-184X>  
 Mayank Narang  <https://orcid.org/0000-0002-0554-1151>  
 Manoj Puravankara  <https://orcid.org/0000-0002-3530-304X>  
 B. Shridharan  <https://orcid.org/0000-0002-2585-0111>  
 H. Tyagi  <https://orcid.org/0000-0002-9497-8856>  
 Bihan Banerjee  <https://orcid.org/0000-0001-8075-3819>  
 Prasanta K. Nayak  <https://orcid.org/0000-0002-4638-1035>  
 Arun Surya  <https://orcid.org/0000-0002-9967-0391>

## References

- Andersson, A., Fender, R. P., Lintott, C. J., et al. 2022, *MNRAS*, **513**, 3482  
 Andrae, R., Fouesneau, M., Sordo, R., et al. 2023, *A&A*, **674**, A27  
 Antonova, A., Hallinan, G., Doyle, J. G., et al. 2013, *A&A*, **549**, A131  
 Banerjee, B., Narang, M., Manoj, P., et al. 2024, *AJ*, **168**, 7  
 Baraffe, I., & Chabrier, G. 2018, *A&A*, **619**, A177  
 Becker, R. H., White, R. L., & Helfand, D. J. 1995, *ApJ*, **450**, 559  
 Benz, A. O., & Güdel, M. 2010, *ARA&A*, **48**, 241  
 Benz, A. O., & Guedel, M. 1994, *A&A*, **285**, 621  
 Berger, E. 2002, *ApJ*, **572**, 503  
 Best, W. M. J. 2020, The UltracoolSheet: Photometry, Astrometry, Spectroscopy, and Multiplicity for 3000+ Ultracool Dwarfs and Imaged Exoplanets, v1.0.1, Zenodo, doi:10.5281/zenodo.4570814  
 Bieging, J. H., Abbott, D. C., & Churchwell, E. B. 1989, *ApJ*, **340**, 518  
 Bookbinder, A. J. 1988, *Activity in Cool Star Envelopes* (Dordrecht: Kluwer), 143  
 Brown, A. G. A., Vallenari, A., Prusti, T., et al. 2018, *A&A*, **616**, A1  
 Burningham, B., Hardcastle, M., Nichols, J. D., et al. 2016, *MNRAS*, **463**, 2202  
 Callingham, J. R., Vedantham, H. K., Shimwell, T. W., et al. 2021, *NatAs*, **5**, 1233  
 Cauley, P. W., Shkolnik, E. L., Llama, J., & Lanza, A. F. 2019, *NatAs*, **3**, 1128  
 Ceballos, K. N. O., Cendes, Y., Berger, E., & Williams, P. K. G. 2024, *AJ*, **168**, 127  
 Chabrier, G., & Baraffe, I. 2000, *ARA&A*, **38**, 337  
 Condon, J. J., Cotton, W. D., Greisen, E. W., et al. 1998, *AJ*, **115**, 1693  
 Das, B., Chandra, P., Shultz, M. E., et al. 2022, *ApJ*, **925**, 125  
 Das, B., Chandra, P., Wade, G. A., Shultz, M. E., & Sikora, J. 2020, in *Stellar Magnetism: A Workshop in Honour of the Career and Contributions of John D.*, ed. G. Wade (Warsaw: Polish Astronomical Society), 66  
 Davis, I., Vedantham, H. K., Callingham, J. R., et al. 2021, *A&A*, **650**, L20  
 Donati, J. F., & Landstreet, J. D. 2009, *ARA&A*, **47**, 333  
 Dorman, B., Nelson, L. A., & Chau, W. Y. 1989, *ApJ*, **342**, 1003  
 Doyle, L., Ramsay, G., Doyle, J. G., & Wu, K. 2019, *MNRAS*, **489**, 437  
 Driessen, L. N., Heald, G., Duchesne, S. W., et al. 2023, *PASA*, **40**, e036  
 Driessen, L. N., Pritchard, J., Murphy, T., et al. 2024, *PASA*, **41**, e084  
 Driessen, L. N., Williams, D. R. A., McDonald, I., et al. 2021, *MNRAS*, **510**, 1083  
 Dulk, G. A. 1985, *ARA&A*, **23**, 169  
 Feeney-Johansson, A., Purser, S. J. D., Ray, T. P., et al. 2021, *A&A*, **653**, A101  
 Frasca, A., Guillout, P., Klutsch, A., et al. 2018, *A&A*, **612**, A96  
 Gaia Collaboration, Smart, R. L., Sarro, L. M., et al. 2021, *A&A*, **649**, A6  
 Gaia Collaboration, Vallenari, A., Brown, A. G. A., et al. 2023, *A&A*, **674**, A1  
 Galli, P. A. B., Loinard, L., Ortiz-Léon, G. N., et al. 2018, *ApJ*, **859**, 33  
 Goldreich, P., & Lynden-Bell, D. 1969, *ApJ*, **156**, 59  
 Gordon, Y. A., Boyce, M. M., O'Dea, C. P., et al. 2020, *RNAAS*, **4**, 175  
 Grießmeier, J.-M. 2015, in *ASSL 411, Characterizing Stellar and Exoplanetary Environments*, ed. H. Lammer & M. Khodachenko (Berlin: Springer), 213  
 Gudel, M. 2002, *ARA&A*, **40**, 217  
 Gudel, M., Schmitt, J. H. M. M., Bookbinder, J. A., & Fleming, T. A. 1993, *ApJ*, **415**, 236  
 Intema, H. T., Jagannathan, P., Mooley, K. P., & Frail, D. A. 2017, *A&A*, **598**, A78  
 Jao, W.-C., Henry, T. J., Gies, D. R., & Hambly, N. C. 2018, *ApJL*, **861**, L11  
 Kao, M., Hallinan, G., Pineda, J. S., et al. 2017, *AAS Meeting Abstracts*, 229, 408.06  
 Kavanagh, R. D., Vidotto, A. A., Klein, B., et al. 2021, *MNRAS*, **504**, 1511  
 Kimball, A. E., & Ivezić, U. 2008, *AJ*, **136**, 684  
 Kimball, A. E., Knapp, G. R., Ivezić, Z., et al. 2009, *ApJ*, **701**, 535  
 Kovari, Z., Strassmeier, K. G., Kriskovics, L., et al. 2024, *A&A*, **684**, A94  
 Lacy, M., Baum, S. A., Chandler, C. J., et al. 2020, *PASP*, **132**, 035001  
 Lecavelier Des Etangs, A., Sirothia, S. K., Gopal-Krishna, & Zarka, P. 2011, *A&A*, **533**, A50  
 Leone, F., Umama, G., & Triglio, C. 1996, *A&A*, **310**, 271  
 McConnell, D., Hale, C. L., Lenc, E., et al. 2020, *PASA*, **37**, e048  
 Morris, D. H., & Mutel, R. L. 1988, *AJ*, **95**, 204  
 Mutel, R. L., Lestrade, J. F., Preston, R. A., & Phillips, R. B. 1985, *ApJ*, **289**, 262  
 Narang, M. 2022, *MNRAS*, **515**, 2015  
 Narang, M., Manoj, P., & Ishwara Chandra, C. H. 2021, *RNAAS*, **5**, 158  
 Narang, M., Manoj, P., Ishwara Chandra, C. H., et al. 2020, *MNRAS*, **500**, 4818  
 Narang, M., Oza, A. V., Hakim, K., et al. 2023a, *AJ*, **165**, 1  
 Narang, M., Oza, A. V., Hakim, K., et al. 2023b, *MNRAS*, **522**, 1662  
 Narang, M., Puravankara, M., Chandra, C. H. I., et al. 2024, *MNRAS*, **529**, 1161  
 Noyola, J. P., Satyal, S., & Musielak, Z. E. 2014, *ApJ*, **791**, 25  
 Pecaut, M. J., & Mamajek, E. E. 2013, *ApJS*, **208**, 9  
 Pritchard, J., Murphy, T., Zic, A., et al. 2021, *MNRAS*, **502**, 5438  
 Reiners, A., & Basri, G. 2009, *A&A*, **496**, 787  
 Rengelink, R. B., Tang, Y., de Bruyn, A. G., et al. 1997, *A&AS*, **124**, 259  
 Rizzuto, A. C., Mann, A. W., Vanderburg, A., Kraus, A. L., & Covey, K. R. 2017, *AJ*, **154**, 224  
 Semenko, E. A., Romanyuk, I. I., Kudryavtsev, D. O., & Yakunin, I. A. 2014, *AstBu*, **69**, 191  
 Shimwell, T. W., Röttgering, H. J. A., Best, P. N., et al. 2017, *A&A*, **598**, A104  
 Shkolnik, E., Bohlender, D. A., Walker, G. A. H., & Collier Cameron, A. 2008, *ApJ*, **676**, 628  
 Team, T. C., Bean, B., Bhatnagar, S., et al. 2022, *PASP*, **134**, 114501  
 Toet, S. E. B., Vedantham, H. K., Callingham, J. R., et al. 2021, *A&A*, **654**, A21  
 Townsend, R. H. D., Rivinius, T., Rowe, J. F., et al. 2013, *ApJ*, **769**, 33  
 Triglio, C., Biswas, A., Leto, P., et al. 2023, arXiv:2305.00809  
 Vedantham, H. K. 2020, *MNRAS*, **500**, 3898  
 Vedantham, H. K., Callingham, J. R., Shimwell, T. W., et al. 2020, *NatAs*, **4**, 577  
 Vedantham, H. K., Callingham, J. R., Shimwell, T. W., et al. 2022, *ApJL*, **926**, L30  
 Walter, F. M., Beck, T. L., Morse, J. A., & Wolk, S. J. 2003, *AJ*, **125**, 2123  
 Wayth, R. B., Lenc, E., Bell, M. E., et al. 2015, *PASA*, **32**, e025  
 Webb, N. A., Coriat, M., Traulsen, I., et al. 2020, *A&A*, **641**, A136  
 Webb, N. A., Coriat, M., Traulsen, I., et al. 2023, *yCat*, **IX/69**  
 Wenger, M., Ochsenein, F., Egret, D., et al. 2000, *A&AS*, **143**, 9  
 Willes, A. J., & Wu, K. 2005, *A&A*, **432**, 1091  
 Wright, A. E., & Barlow, M. J. 1975, *MNRAS*, **170**, 41  
 Yiu, T. W. H., Vedantham, H. K., Callingham, J. R., & Günther, M. N. 2024, *A&A*, **684**, A3  
 Zhang, L., Pi, Q., Han, X. L., Chang, L., & Wang, D. 2016, *MNRAS*, **459**, 854